Liu *et al. Biochar* (2022) 4:47
https://doi.org/10.1007/s42773-022-00172-z

Biochar

ORIGINAL RESEARCH Open Access

Stability and interaction of biochar and iron mineral nanoparticles: effect of pH, ionic strength, and dissolved organic matter

Yong Liu[1,2], Jie Ma[1,2*], Jiaoli Gao[3], Xingyi Chen[3], Xiaoxue Ouyang[1,2], Liping Weng[1,2,4*], Haiming Li[5], Yali Chen[1,2] and Yongtao Li[6,7]

Abstract

Biochar nanoparticles (BCNPs) and iron mineral nanoparticles (IMNPs), such as ferrihydrite nanoparticles (FHNPs), magnetite nanoparticles (MTNPs), and goethite nanoparticles (GTNPs), are often combined and used in soil remediation. However, the stability and interaction of nanoparticles under various environmental conditions have not been investigated previously. In this study, settling experiments, a semi-empirical model, the Derjaguin–Landau–Verwey–Overbeek (DLVO) theory, scanning electron microscopy (SEM) observations, and quantum chemical calculations were used to study the interaction and heteroaggregation of BCNPs and IMNPs. Settling of BCNPs-FHNPs and BCNPs-GTNPs was stable at neutral and alkaline pH (relative concentration of unsettled nanoparticles $C_{res'} = 0.679–0.824$), whereas fast settling of BCNPs-IMNPs was observed at acidic pH ($C_{res'} = 0.104–0.628$). By contrast, BCNPs-MTNPs consistently showed moderate settling regardless of the mass of magnetite at all pH ($C_{res'} = 0.423–0.673$). Both humic acid (HA, 10 mg L^{-1}) and ionic strength (IS, 10 and 100 mM) facilitated the settling of BCNPs-FHNPs and BCNPs-MTNPs systems, whereas the settling of BCNPs-GTNPs was sensitive only to IS. Fulvic acid (10 mg L^{-1}) had a general stabilizing effect on the BCNPs-IMNPs systems. The results of SEM and quantum chemical calculations suggested that the interaction between BCNPs and FHNPs (-2755.58 kJ mol^{-1}) was stronger than that between BCNPs and GTNPs (−1706.23 kJ mol^{-1}) or MTNPs (−1676.73 kJ mol^{-1}). The enhancement of heteroaggregation between BCNPs and IMNPs under unfavorable conditions (acidic pH, HA, and IS) was regulated by the strength of the interaction. Therefore, the enhancement of heteroaggregation of BCNPs-FHNPs was greater than that of BCNPs-MTNPs. In the BCNPs-GTNPs system, the high concentration and elongated structure of GTNPs may contribute greatly to heteroaggregation and settling with small interactions. Our results highlight the influence of pH, IS, and HA on the interaction between BCNPs and IMNPs. These results will be helpful in the application of BCNPs and IMNPs for soil remediation.

Highlights

- The type of iron minerals regulated the stability of BCNPs-IMNPs.
- FHNPs were was most closely combined with BCNPs, followed by GTNPs and MTNPs.
- Unfavorable conditions enhanced the settling of BCNPs-FHNPs.
- The settling of BCNPs-FHNPs was insensitive to environmental conditions.

*Correspondence: majie@caas.cn; wengliping@caas.cn

[1] Key Laboratory for Environmental Factors Control of Agro-Product Quality Safety, Ministry of Agriculture and Rural Affairs, Tianjin 300191, China
Full list of author information is available at the end of the article

- High concentration of elongated GTNPs contributed to the settling of BCNPs-GTNPs.

Keywords: Biochar, Iron mineral nanoparticles, Stability, DLVO, Quantum chemistry

Graphical Abstract

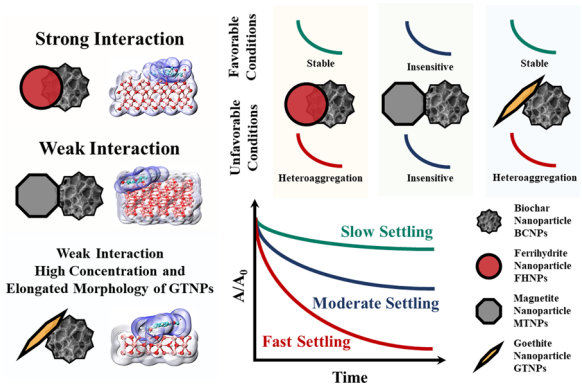

1 Introduction

Biochar (BC) is a pyrolysis product of the thermal decomposition of organic matter (Ahmad et al. 2012). It is widely used in the remediation of soil pollution (O'Connor et al. 2018; Qiu et al. 2022). However, the adsorption capacity of pristine BC is limited owing to the defects in its surface structure (Jung et al. 2018; Wang et al. 2015). Iron oxides are often used to modify BC and improve its adsorption capacity (Wan et al. 2020). Numerous studies have found that iron-modified BC is beneficial for the passivation of heavy metals in soil (Gholizadeh and Hu 2021; Liu et al. 2022b). For instance, a study reported that iron-based BC composites can effectively repair Cr-contaminated soil and reduce toxicity and migration of Cr in soil (Chen et al. 2021). Similarly, the application of goethite (GT)-modified BC to Cd- and As-contaminated paddy soil drastically reduced the accumulation of Cd and As in rice tissues (Irshad et al. 2020). Nanosized BC and ferrihydrite (FH) complexes have also been reported to adsorb Cd and As in the rhizosphere soil and pore water, thereby preventing the uptake of Cd and As by *Brassica chinensis* L. roots (Ouyang et al. 2021). The use of magnetic BC can reduce the amounts of Cd, Zn, and Cu in acid-extracted soil by 8–10%, 27–29%, and 59–63%, respectively (Lu et al. 2018). Furthermore, nano zero-valent iron-modified BC can effectively enhance Cr immobilization in Cr-contaminated soil (Liu et al. 2020; Su et al. 2016).

Iron minerals exist in abundance in soil even if they are not externally added to soil as remediation materials. Their main forms in soil include FH, magnetite (MT), and GT (Clarr van der Zee et al. 2003) which can transform into one another (Ma et al. 2020; Nielsen et al. 2014; Schwertmann et al. 2018). For example, GT is the most prominent product of FH transformation under acidic or alkaline conditions (Schwertmann et al. 2018) over several years of aging (Nielsen et al. 2014). In addition, the core–shell structure of zero-valent iron in soil gradually dissolves, collapses, and agglomerates on the surface of clay minerals, and the main oxidation product is crystalline MT (Wang et al. 2021).

Iron oxides preferentially exist as small particles or nanoparticles in soil (Ivanić et al. 2016); among them, ferrihydrite nanoparticles (FHNPs) have been widely investigated (Vodyanitskii and Shoba 2016). In addition, GT is an important nanoscale crystallite found in nearly all soil types (Till et al. 2015). Aggregation of magnetite nanoparticles (MTNPs) has been reported in red soils (Zhang et al. 2020). Moreover, engineered iron-based nanoparticles have also been introduced into the soil because they are widely used for treating pollutants in soil (Baragaño et al. 2020; Zhou et al. 2012).In addition, BC, which is used to mitigate heavy metal pollution in soil (Zhu et al. 2020), also forms nanoparticles when added to soil. A previous study has reported the transport of BC nanoparticles (BCNPs) in acidic and alkaline soils (Chen et al. 2018). Both iron minerals and BC form nanoparticles and interact with each other when they coexist in the soil environment (Wan et al. 2020). Many studies have underlined the importance of understanding the transformations of nanomaterials following their release into the environment, such as aggregation, dissolution, and interactions, which eventually alter their fate and the potential toxicity associated with pollutants (Dwivedi and Ma

2014; Lin et al. 2010; Mitrano et al. 2015). Among these, aggregation is the most important (Hotze et al. 2010).

The stability of BC and iron mineral nanoparticles (IMNPs) is affected by soil pH, organic matter content, and ionic strength (IS) (Chen et al. 2019; Ma et al. 2015; Tosco et al. 2012; Wang et al. 2021). Previous studies have shown that a mixture of GTNPs and FHNPs condenses rapidly with an increase in pH and the presence of humic acid (HA) (Ma et al. 2020). Similarly, the transport of BCNPs decreased with decreasing pH (Zhang et al. 2010). Moreover, the transport of BCNPs generally increased with increasing hunic acid (HA) concentrations (Chen et al. 2017). This stabilization effect was substantially improved with increasing HA concentration and pH (Hu et al. 2010). The increased IS of the solution considerably reduced the transport of NPs, thereby reducing the potential of NPs-mediated pollutant transport (Fang et al. 2016). A high IS (e.g., 10 mM) in an aquifer can reduce the movement of FHNPs to a few meters, unlike that in natural flow conditions (2–5 m) (Tosco et al. 2012). A small dose (2 mg L^{-1}) of HA greatly stabilized the MTNPs suspension at a high IS (Hu et al. 2010). In addition, BC can interact with a wide range of iron minerals in the soil (Joseph et al. 2010). On the one hand, the close binding of iron minerals to the surface of BC will form organometallic complexes (e.g., Fe−O−C), which change the surface properties of BC (Yang et al. 2016). However, BC can also act as an electron shuttle to promote the reduction of Fe(III) oxides (e.g., FH and hematite), thus improving the yield of Fe(II) adsorbed species, changing the secondary mineral phase, and generating BC-mineral composites (Kappler et al. 2014; Xu et al. 2016). When nanoparticles are in a relatively stable state, they may transport or carry inherent contaminants along the soil profile, posing a risk to the groundwater.

Although the environmental behavior of non-coexisting iron minerals and BCNPs has been extensively studied, the stability and interaction of BC and IMNPs, and the influence of various factors on their coexistence conditions have not been systematically studied. This study investigated the stability of the coexistence of iron minerals and BCNPs and the impact of environmental factors using a settlement test and dynamic model, and the interaction mechanism of nanoparticles was revealed by scanning electron microscopy and quantum chemical calculation.

2 Materials and methods

2.1 Preparation of Fe oxide minerals and biochar

Ferrihydrite was synthesized by titrating the dissolved $Fe(NO_3)\cdot 9H_2O$ with KOH to a pH of 7.5 (Schwertmann and Cornell 2008). Magnetite was synthesized by adding 0.5 M $FeSO_4\cdot 7H_2O$ (Sinopharm Chemical Reagent Co. Ltd.) to a mixed solution of 0.27 M KNO_3 and 3.3 M KOH with nitrogen purging at 90 °C for 45 min (Schwertmann and Cornell 2008). Goethite was precipitated by titrating the dissolved $Fe(NO_3)_3\cdot 9H_2O$ (Sinopharm Chemical Reagent Co. Ltd.) with KOH to a pH of 12 (Schwertmann and Cornell 2008). The mixed suspension was aged for four days and dialyzed until it was free from electrolytes. The particle sizes (partially agglomerate state) of FHNPs, MTNPs, and GTNPs were 198.5 ± 12.6, 226.5 ± 22.4, and 383.2 ± 35.1, respectively, and the crystal forms of these nanoparticles have been reported using X-ray diffraction in previous studies (Liu et al. 2022a; Ma et al. 2020). The BC used in the present study was obtained by pyrolyzing wheat straw at 300 °C for 2 h and cooling it to 25 °C using whole-course protection in an N_2 atmosphere. Thereafter, the obtained BC was sonicated in 6 M HCl solution to remove acid-soluble oxides, and then repeatedly washed with ultrapure water until the conductivity of the filtrate was 5.0 μS cm^{-1} (Ouyang et al. 2021). The pH of the BC was 10.1, and the pore size distribution ranged from 10 to 100 μm with a specific surface area of 2.1 $m^2\ g^{-1}$ (Qian et al. 2020). We determined the infrared characteristics of BC in a previous study. Peaks obtained at 3341, 1733, 1666, and (1411, 1158, and 850) cm^{-1} represented the O–H, C=O, (C=O and C=C), and C-H stretching vibrations, respectively; this proved that it was a typical BC (Liu et al. 2022a; Ma et al. 2022). After freeze-drying, the materials were ground to produce a fine powder for subsequent experiments.

2.2 Settling experiments

Settling experiments were conducted in duplicate for pure BCNPs and mixtures of nanoparticles (BCNPs and IMNPs) under varying conditions of iron mineral pH, IS, and dissolved organic matter (DOM) for 1200 min in a spectrophotometric cuvette. The experimental conditions are presented in Additional file 1: Table S1. The suspensions of nanoparticles were prepared by adding iron minerals (0, 0.02, and 0.05 g, respectively) and 0.1 g of BC to 40 mL of Milli-Q water. The BC and IM contents of the suspensions were based on the common proportion in iron-modified BC. The pH of the suspensions was carefully adjusted using small amounts of 0.1 M NaOH or HCl solutions, and the IS was adjusted using 1–10 M NaCl solution to specific experimental values. Commercial HA and fulvic acid (FA) (Sinopharm Chemical Reagent Co. Ltd.) were used to prepare DOM. The solutions were sonicated for 60 min, followed by shaking for 20 h, and then sonicated again for 30 min. The supernatant was then siphoned off and used immediately after it was siphoned. The settling rate was measured using 3 mL of the supernatant in a spectrophotometer (UV-2700, Shimadzu) at 315 nm. The size and zeta potential of the

nanoparticles were measured using a dynamic light scattering analyzer (Zetasizer Nano ZS, Malvern) (Additional file 1: Table S1). The iron concentration in the suspension was measured using atomic absorption spectroscopy (AAnalyst 900 T, PerkinElmer) after HCl digestion (Additional file 1: Table S1).

2.3 Estimation of settling rates

The settling data were interpreted using a semi-empirical model that provided the nanoparticle concentration in the supernatant (C_t) as a function of time (Quik et al. 2014; Velzeboer et al. 2014), as given in Eq. 1:

$$C_t = C_{res} + (C_0 - C_{res})\exp[-\left(\frac{V_s}{h} + K_{diss}\right)t] \quad (1)$$

where C_t is the nanoparticle concentration at time t, C_{res} is the concentration of unsettled nanoparticles at infinite time, C_0 is the initial concentration, V_s (mm h^{-1}) is the settling rate, h is the settling length (distance from the water surface to where samples were taken; 10 mm, spectrophotometer test position), K_{diss} is the dissolution rate constant, and t is the settling time.

C_t, C_{res}, and C_0 represent the value of relative concentrations and C_t/C_0, C_{res}/C_0, and $C_0/C_0 = 1$. Only trace amounts of dissolved Fe (< 10 μg L^{-1}) were detected during the settling experiments, indicating that the dissolutions of iron minerals were negligible (Ma et al. 2020). Therefore, K_{diss} can be ignored in this study. Equation 2 was obtained by integrating Eq. 1, as follows:

$$\frac{C_t}{C_0} = \frac{C_{res}}{C_0} + \left(1 - \frac{C_{res}}{C_0}\right)\exp[-(100V_s)t] \quad (2)$$

2.4 Calculation of DLVO energy

The interaction energy between the nanoparticles (sphere-sphere) was determined by the Derjaguin-Landau-Verwey-Overbeek (DLVO) theory (Derjaguin and Landau 1993; Verwey 1947). The DLVO theory states that the total interaction energy is determined as the arithmetic sum of the Van der Waals attractive energy (E_{VDW}) and electrical double layer energy (E_{EDL}), as given in Eq. 3:

$$E_{TOT} = E_{VDW} + E_{EDL} \quad (3)$$

The E_{VDW} between nanoparticles in water was evaluated according to Eq. 4 (Zhao et al. 2014), as follows:

$$E_{VDW} = -\frac{Ar_1r_2}{6h(r_1+r_2)}\left[1 - \frac{5.32h}{\lambda}\ln\left(1 + \frac{\lambda}{5.32h}\right)\right]^{-1} \quad (4)$$

where A is the Hamaker constant, which was estimated as 5.5×10^{-20} J (Blakey and James 2003), 5.0×10^{-20} J (Tosco et al. 2012), 2.3×10^{-19} J (Buske 1994), and 6.19×10^{-20} J (Wang et al. 2013; Yang et al. 2017) for the pure GTNPs, FHNPs, MTNPs, and BCNPs systems, respectively. In a mixed system, the Hamaker constants were estimated as their arithmetic mean. r_1 and r_2 are the hydrodynamic radius of nanoparticles, h is the separation distance between nanoparticles, and λ is the characteristic wavelength of interaction (100 nm) (Gregory 1981).

The E_{EDL} is a function of the separation distance between nanoparticles immersed in water (Zhao et al. 2014), as given in Eq. 5:

$$E_{EDL} = \frac{2\pi r_1 r_2 n_\infty kT}{(r_1+r_2)\kappa^2}(\psi_1^2+\psi_2^2)\left\{\frac{2\psi_1\psi_2}{\psi_1^2+\psi_2^2}\ln\left[\frac{1+\exp(-\kappa h)}{1-\exp(-\kappa h)}\right] + \ln[1-\exp(-2\kappa h)]\right\} \quad (5)$$

where ψ_1 and ψ_2 are the zeta potentials of nanoparticles (mV) used to approximate the surface potential, n_∞ is the number density of ions (m^{-3}), k is the Boltzmann constant (1.38×10^{-23} J K^{-1}), T is the absolute temperature (298 K), and κ is the Debye–Huckel parameter (m^{-1}). The Debye–Huckel parameter is also an estimation of the effective thickness of the electrical double layer calculated according to Eq. 6:

$$\kappa = 3.28 \times (I)^{1/2} \times 10^9 \quad (6)$$

where I is ionic strength.

The hydrodynamic radius and zeta potential of the individual nanoparticles in the mixed systems were unknown in the mixed systems. Instead, values were approximated based on the properties of the BCNPs-IMNPs (Additional file 1: Table S1). Although the calculation methods of hydrodynamic radius, zeta potential, and Hamaker constant have some limitations, the above DLVO calculations can be used to estimate the approximate changes in average interaction energy.

2.5 SEM observations

The micro-morphological characteristics of separate as well as mixed (0.1 g of BC and 0.02 g iron minerals) nanoparticles at pH 7.0 and time of 200 min were investigated using scanning electron microscopy (SEM, MIRA LMS, Tescan) coupled with energy dispersive X-ray spectroscopy (EDS, Xplore 30) mapping images. A platinum coating and silicon substrate were not used to avoid any influence on the EDS analysis. To avoid excessive stacking

between nanoparticles, the suspension was diluted four times by background solution. For SEM imaging, 2 μL of the diluted suspension was dropped onto a piece of silicon slice. The area of the silicon slice covered by the droplet was 3.14 mm^2 and immediately vacuum freeze-dried using a vacuum freeze-drier.

2.6 Quantum chemical calculation

Quantum chemical calculations can compensate for interactions that cannot be explained using colloidal chemistry (Ma et al. 2022). To investigate the interactions between BCNPs and IMNPs, modified molecular structure of BC (Tian et al. 2020) and crystal structures of FH (Chappell et al. 2017), MT (Liu et al. 2019a), and GT (Russell et al. 2009) were constructed. Their molecular formulas are shown in Additional file 1: Fig. S1. The configurations of the complexes were determined using Molclus (Lu 2021). Two hundred original configurations were generated, and each configuration was optimized based on Parameterized Model 6 using Gaussian 16 (Frisch et al. 2016). Then, the single-point energy of the first configuration with the lowest energy was calculated at the B3LYP/6-31G(d) level, in which element was adopted as the Lanl2DZ basis set. Grimme's D3BJ dispersion was used to describe the intermolecular interactions in all calculations. The binding energies between different BC molecular and crystal structures of the iron minerals were calculated using Eq. 7:

$$\text{Binding energy} = \text{Ecomplex} - \left(\text{Efragment1} + \text{Efragment2}\right); \quad (7)$$

where $E_{complex}$ represents the energy of a complex composed of two molecules, and $E_{Fragment1}$ and $E_{Fragment2}$ represent the energy of a single molecule (crystal) corresponding to different systems.

To demonstrate the nature of the interaction more clearly, the electrostatic potential (ESP) was analyzed using Multiwfn software (Lu and Chen 2012). All visualizations of the complex structures and contour surfaces of the ESP were drawn using VMD software (Humphrey et al. 1996).

3 Results and discussion

3.1 Effects of environmental conditions on BCNPs settling

The settling kinetics and Derjaguin–Landau–Verwey–Overbeek (DLVO) energies of the BCNPs under varying conditions, as well as the calculation results of the corresponding models, are given in Fig. 1 and Additional file 1: Table S2, and the DLVO calculation parameters are provided in Additional file 1: Table S1. The stability of the BCNPs increased with increasing pH (Fig. 1a), as indicated by the decrease in V_s of the BCNPs from 1.05 to 0.51 mm h^{-1} with increasing pH (Additional file 1: Table S2). The value of V_s was the lowest at pH 10.0 (Additional file 1: Table S2), which indicated slow settling of BCNPs. However, C_{res}, remained relatively stable (0.273–0.374) under all pH conditions (Additional file 1: Table S2), demonstrating that pH has little effect on the proportion of stable BCNPs.

At pH 7.0, HA had a little effect on the settling of BCNPs (Fig. 1a). However, FA (10 mg L^{-1}) contributed to the stabilization of BCNPs ($V_s = 0.47$ mm h^{-1}) and had a stronger stabilizing effect than HA ($V_s = 0.73$ mm h^{-1}) (Fig. 1a and Additional file 1: Table S2). Dissolved organic matter can act as a steric barrier layer, thereby resulting in stabilization of nanoparticles (Ma et al. 2018; Philippe and Schaumann 2014; Xu et al. 2021). Considering steric hindrance, HA with large molecular volume should contribute more to the systemic stability than FA with small molecular volume. However, FA molecules have

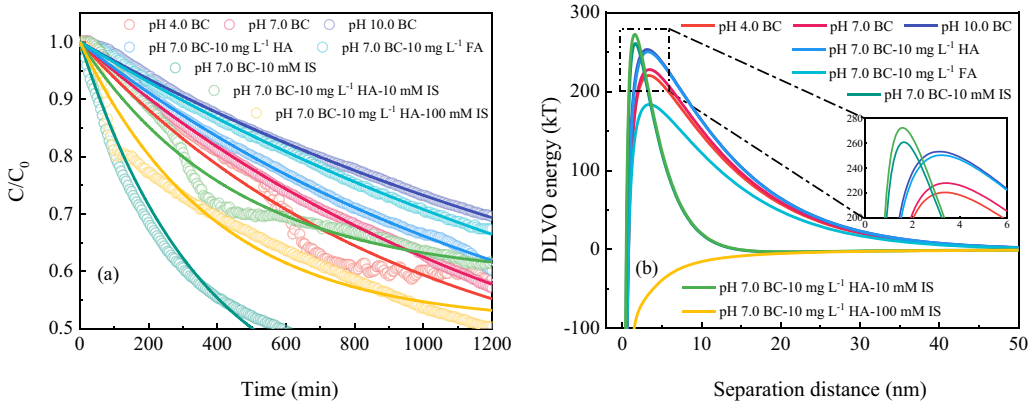

Fig. 1 Settling kinetics (**a** symbols indicate observed data points and lines indicate simulation fitting) and DLVO energies (**b**) of the BCNPs with varying conditions (pH, IS, and DOM)

more carboxylate and hydroxy functional groups (Islam et al. 2020); in addition, the average location of the reactive groups is closer to the molecular surface in FA than that in HA (Weng et al. 2006). Moreover, the relatively low negative zeta potential of FA compared to that of HA (Klucakova 2018) is more favorable for FA binding to BCNPs with a high negative zeta potential (Ma et al. 2022; Ouyang et al. 2021; Qian et al. 2020).

Ionic strength had a great effect on the settling of BCNPs, and the stability of BCNPs decreased with the addition of IS (10 mM NaCl) at pH 7.0, as evidenced by the high V_s value of 2.83 mm h^{-1} (Fig. 1 and Additional file 1: Table S2). The V_s values of BCNPs decreased from 2.83 to 2.22 mm h^{-1} when HA was present in 10 mM IS. This indicates that HA improves the stability of BCNPs under specific IS conditions (Chen et al. 2022b). Similarly, in this case, the stability of BCNPs slightly decreased (V_s increased from 2.22 to 2.57 mm h^{-1}) with increasing IS (from 10 to 100 mM) (Fig. 1 and Additional file 1: Table S2). However, it was more stable under this condition (10 mg L^{-1} HA with 100 mM IS) than under the 10 mM IS condition. This indicates that a higher IS promotes the settling of BCNPs, and the stabilizing effect of HA is still reflected.

The DLVO calculation results are given in Fig. 1b, and the calculation parameters are provided in Additional file 1: Table S1. Most of the primary barriers under different conditions were greater than 183 kT (Fig. 1b and Additional file 1: Table S2) owing to the negative zeta potential (from −38.97 to −51.47 mV) and appropriate particle size (from 561.1 to 673.6 nm) (Additional file 1: Table S1). The range of change in particle size was smaller than that of zeta potential change, which indicates that zeta potential change had a greater influence on the stability of BCNPs than particle size. The tendency toward settling (at pH 7.0 with 100 mM IS and 10 mg L^{-1} HA) suggested that the primary energy barrier was absent (Fig. 1b and Additional file 1: Table S2) owing to the high IS. Moderate IS conditions did not decrease the primary energy barrier (Fig. 1b and Additional file 1: Table S2), but slightly increased it, which was attributed to the increase in particle size (Additional file 1: Table S1). However, the influence of the IS led to relatively rapid settling of the BCNPs (Fig. 1a). Fulvic acid, with a relatively low negative zeta potential, decreased the negative potential of the system (Additional file 1: Table S1), thereby also decreasing the primary energy barrier. These DLVO results under conditions of IS and FA were not consistent with the stability characteristics, whereas other DLVO results could explain the settling phenomenon of BCNPs. In addition, when the steric hindrance effect is considered, the energy barrier of the system in the presence of HA will increase, resulting in further deviation from the settling results. Therefore, we concluded that the steric repulsion energy could not be used to analyze the stability of BCNPs in the present study.

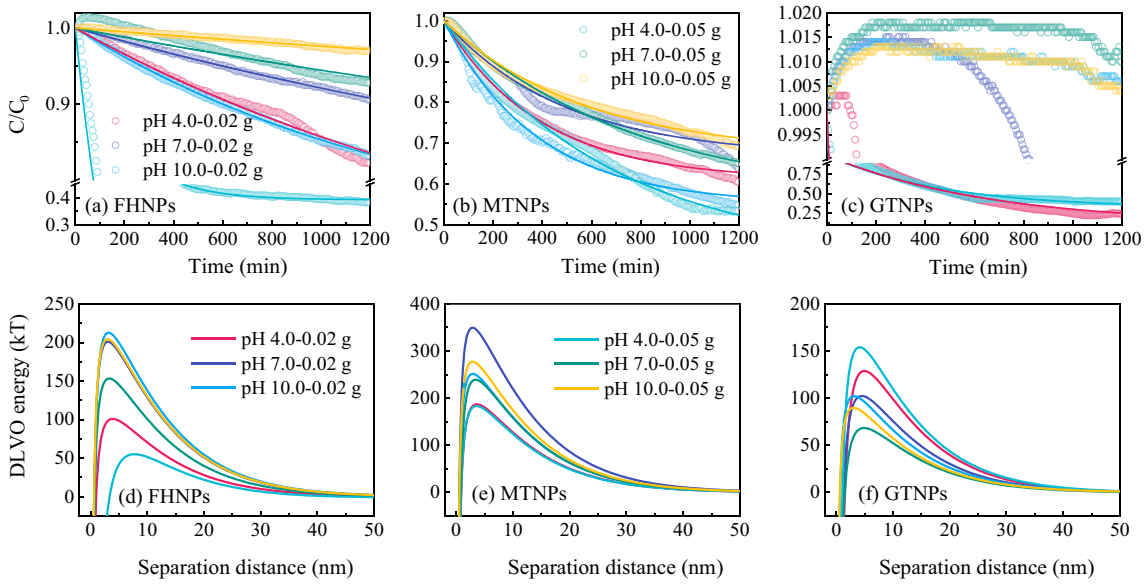

Fig. 2 Settling kinetics (**a**–**c**, symbols indicate observed data points and lines indicate simulation fitting) and DLVO energies (**d**–**f**) of the BCNPs-IMNPs with varying iron mineral contents and pH

3.2 Effects of iron mineral mass and pH on BCNPs-IMNPs settling

The settling kinetics, DLVO energies, and calculation results of the corresponding models of BCNPs-IMNPs mixtures under different masses of IMs are given in Fig. 2 and Additional file 1: Table S3, respectively. Most BCNPs-FHNPs remained stable during settling (Fig. 4a). Compared to individual BCNPs, in general, V_s values of BCNPs-FHNPs showed a decreasing trend and $C_{res'}$ values showed an increasing trend (Figs. 1a and 2a and Additional file 1: Table S2 and S3), which reflects the stability effect of FHNPs on the mixed system. This can be attributed to the potential of the system to maintain high negative values, and the fact that individual FHNPs have high stability under most conditions (Ma et al. 2020), which improves the overall stability. However, under the condition of pH 4.0-FH 0.05 g, V_s and $C_{res'}$ values of BCNPs-FHNPs were 5.39 mm h^{-1} and 0.391, respectively (Fig. 2a and Additional file 1: Table S3). Hence, BCNPs-FHNPs was relatively unstable, owing to the low negative zeta potential (−17.97 mV). Therefore, the primary energy barrier of the BCNPs-FHNPs mixture was only 54.9 kT (Fig. 2d and Additional file 1: Table S3). This led to the aggregation of the nanoparticles after they crossed the low-energy barrier. This is consistent with the TEM, XRD, and DRS results that indicated the coprecipitation of FHNPs and HA at pH 3.5 (Angelico et al. 2014). At low pH, the adsorption of organic matter onto IM was relatively high (Wang et al. 2019). Therefore, we can speculate that the interaction between BCNPs and FHNPs was high at low pH, and that heteroaggregation occurred when FHNPs were at a high concentration (Additional file 1: Table S1). Under the condition of 0.02 g FH, BCNPs-FHNPs was in a relatively stable state at pH 4.0, its V_s and $C_{res'}$ values were 0.48 mm h^{-1} and 0.628, respectively (Fig. 2a and Additional file 1: Table S3). This can be attributed to the low FHNPs concentration (Additional file 1: Table S1). Meanwhile, the primary energy barrier of the BCNPs-FHNPs increased to 100.78 kT. The relatively high energy barrier caused a decrease in the heteroaggregation between BCNPs and FHNPs. In the high FH content system, although the FHNPs concentration increased, BCNPs-FHNPs were in a steady state at neutral and alkaline pH (Fig. 2a and Additional file 1: Table S3) owing to a high negative zeta potential (−39.87 to −43.33 mV) (Additional file 1: Table S1). The BCNPs with high negative zeta potential stabilized the BCNPs-FHNPs system at alkaline pH as the individual FHNPs at pH 10.0 were unstable (Ma et al. 2020), whereas neutralization was observed at acidic pH. The neutralization effect led to a very large particle size of BCNPs-FHNPs, and thus the system quickly completed aggregation stage to settling stage.

In general, BCNPs-MTNPs under each condition maintained a moderately stable state at different pH values (Fig. 2b). Although V_s values of BCNPs-MTNPs increased, $C_{res'}$ values also increased (Additional file 1: Table S2 and S3) at all pH values. These two indicators, which should have changed in the opposite direction, were altered in the same direction. This can likely be attributed to the high rate of initial settling; however, a high proportion of stable BCNPs-MTNPs existed. When the MT content increased from 0.02 to 0.05 g, their V_s values decreased from 2.56 to 1.46 mm h^{-1}, 2.03 to 1.28 mm h^{-1}, and 2.64 to 1.76 mm h^{-1} at different pH (Fig. 2b and Additional file 1: Table S3). This indicated that the high MT content slightly decelerated the preliminary stage of settling of BCNPs-MTNPs. This can be attributed to the settling of individual MTNPs at a slower rate (Vikesland et al. 2016). At pH 4.0 and 7.0, primary energy barriers for 0.05 g MT were 182.97 kT and 238.84 kT, respectively, which were less than those for 0.02 g MT (Fig. 2e and Additional file 1: Table S3). This resulted in a decrease in the concentration of unsettled BCNPs-MTNPs. At pH 10.0, V_s values of the BCNPs-MTNPs (2.64 and 1.76 mm h^{-1}) were higher than at low pH (Additional file 1: Table S3), regardless of MT content (0.02 g or 0.05 g), thereby indicating that the settling of BCNPs-MTNPs was promoted at high pH (Fig. 4b). Compared with individual BCNPs, the MTNPs demonstrated a slight accelerating effect on the settling. In the BCNPs-MTNPs system, although the Fe concentrations were at the same level as in the BCNPs-FHNPs system (Additional file 1: Table S1), the settling characteristics were different. At low pH, there was no rapid settling of BCNPs-MTNPs and clear heteroaggregation.

Settling of BCNPs-GTNPs under different experimental conditions showed an obvious discrepancy (Fig. 2c). Similar to FHNPs, GTNPs stabilized the BCNPs-GTNPs system at neutral and alkaline pH (Fig. 2c). Although BCNPs-GTNPs showed a higher primary energy barrier at pH 4.0 (128.72–153.89 kT) (Fig. 2f), it was relatively unstable. This may be related to the high concentration of the GTNPs and large particle size of BCNPs-GTNPs (Additional file 1: Table S1). The concentration of GTNPs in the suspension was much higher than that of FHNPs and MTNPs. This increased the possibility of an interaction between BCNPs and GTNPs. Although the input of GT (0.02 g) is low, the concentrations of GTNPs (Additional file 1: Table S1) in the mixed system can still be high, which can have a great impact on BCNPs. The large particle size (1013.0 and 749.4 nm, Additional file 1: Table S1) promoted the system to quickly complete the aggregation stage, resulting in settling. At neutral and alkaline pH values, the rate of settling was extremely slow (Fig. 2c and Additional file 1: Table S3); thus, we did not

obtain the fitting parameters. However, similar to the BCNPs-FHNPs system, BCNPs-GTNPs were more stable than individual BCNPs (Fig. 1a) and GTNPs (Ma et al. 2020) at pH 7.0 and 10.0. It can be determined that the BCNPs with high negative zeta potential stabilized the BCNPs-GTNPs system regardless of the GT mass. The settling characteristics of the BCNPs-GTNPs were similar to those of the BCNPs-FHNPs and considerably different from those of the BCNPs-MTNPs.

3.3 Effects of DOM and IS on BCNPs-IMNPs settling

To compare the effects of different environmental conditions on the stability of BCNPs-IMNPs, settling experiments were carried out at pH 7.0 with different concentrations of DOM (HA and FA) and IS. The settling kinetics, DLVO energies, settling parameters, and primary energy barrier of BCNPs-IMNPs mixtures at 7.0 with different concentrations of HA, FA, and IS are given in Fig. 3 and Additional file 1: Table S4. In the presence of HA, the V_s values of the BCNPs-FHNPs were 2.73 mm h^{-1}, much higher than those in the absence of HA, indicating that HA promoted the settling of BCNPs-FHNPs. Although a high primary energy barrier (265.43 kT) was observed (Fig. 3c and Additional file 1: Table S4), the system was not stabilized. The stabilization effect could not be realized by further addition as BC provided a high negative potential and a certain amount of HA (Ma et al. 2022). However, because of the strong adsorption effect on FHNPs (Liu et al. 2019b), added HA was likely to act as a bridge to interface with nanoparticles, thereby enhancing heteroaggregation and settling of BCNPs-FHNPs. Humic acid increases the aggregation of BCNPs via bridging (Yang et al. 2019). In the present study, though IMNPs rarely dissolved, trace amounts of Fe^{2+} or Fe^{3+} may have promoted the formation of metal-bridged ternary complexes (Fe ion-HA-FHNPs) (Yasir et al. 2022). In contrast, FA did not play an obvious bridging role owing to its weak absorption on the FHNPs compared with that of HA (Dublet et al. 2017). However, FA acted as a stabilizer in the BCNPs-FHNPs system, as indicated by the high $C_{res'}$ value (Additional file 1: Table S4). Under 10 mM IS, the V_s values of the BCNPs-FHNPs were around 0.50–0.54 mm h^{-1}, in absence or presence of HA (Additional file 1: Table S4). However, the coexistence of IS and HA ($C_{res'}=0.783$) indicated that BCNPs-FHNPs were relatively stable compared with only 10 mM IS ($C_{res'}=0.611$) or HA ($C_{res'}=0.672$) (Additional file 1: Table S4). This can be attributed to the interaction between IS and HA, which reduced their negative impact on the system. With an increase in IS from 10 to 100 mM with HA, the V_s and $C_{res'}$ values of the BCNPs-FHNPs were 2.35 mm h^{-1} and 0.592 (Fig. 3a and Additional file 1: Table S4), respectively, indicating that high IS significantly promoted the heteroaggregation and settling of BCNPs-FHNPs.

In the BCNPs-MTNPs system, the V_s and $C_{res'}$ values of the BCNPs-MTNPs in the presence of HA were 1.88 mm h^{-1} and 0.544, respectively (Fig. 3b and Additional file 1: Table S4). Although the V_s value decreased compared to that in the absence of HA (Additional file 1:

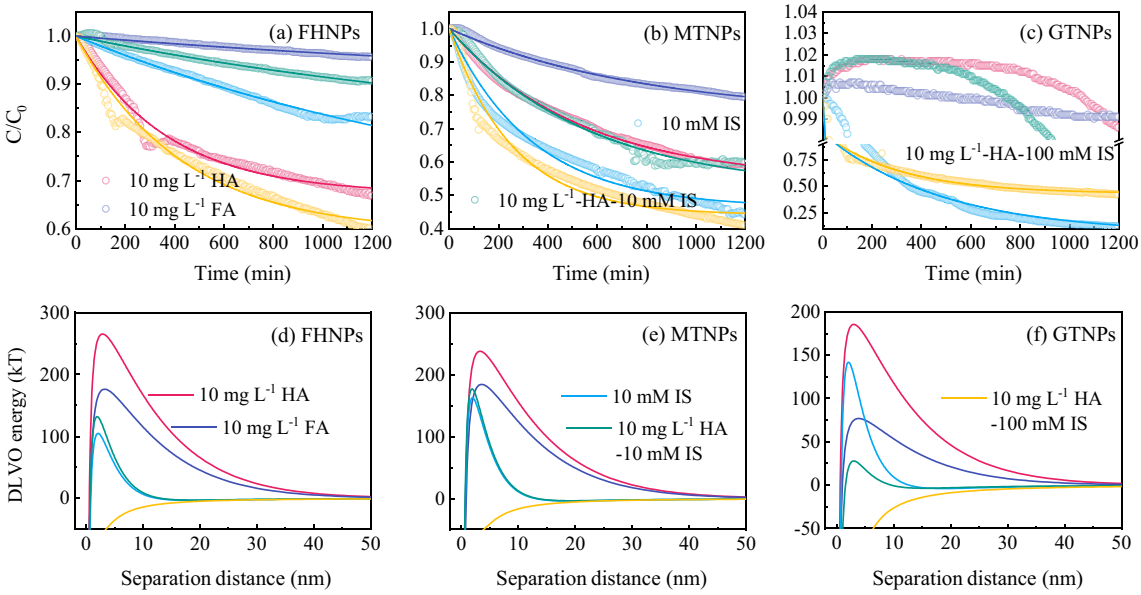

Fig. 3 Settling kinetics (**a**–**c**, symbols indicate observed data points and lines indicate simulation fitting) and DLVO energies (**d**–**f**) of the BCNPs-IMNPs (0.02 g IM) at pH 7.0 with varying DOM species and IS

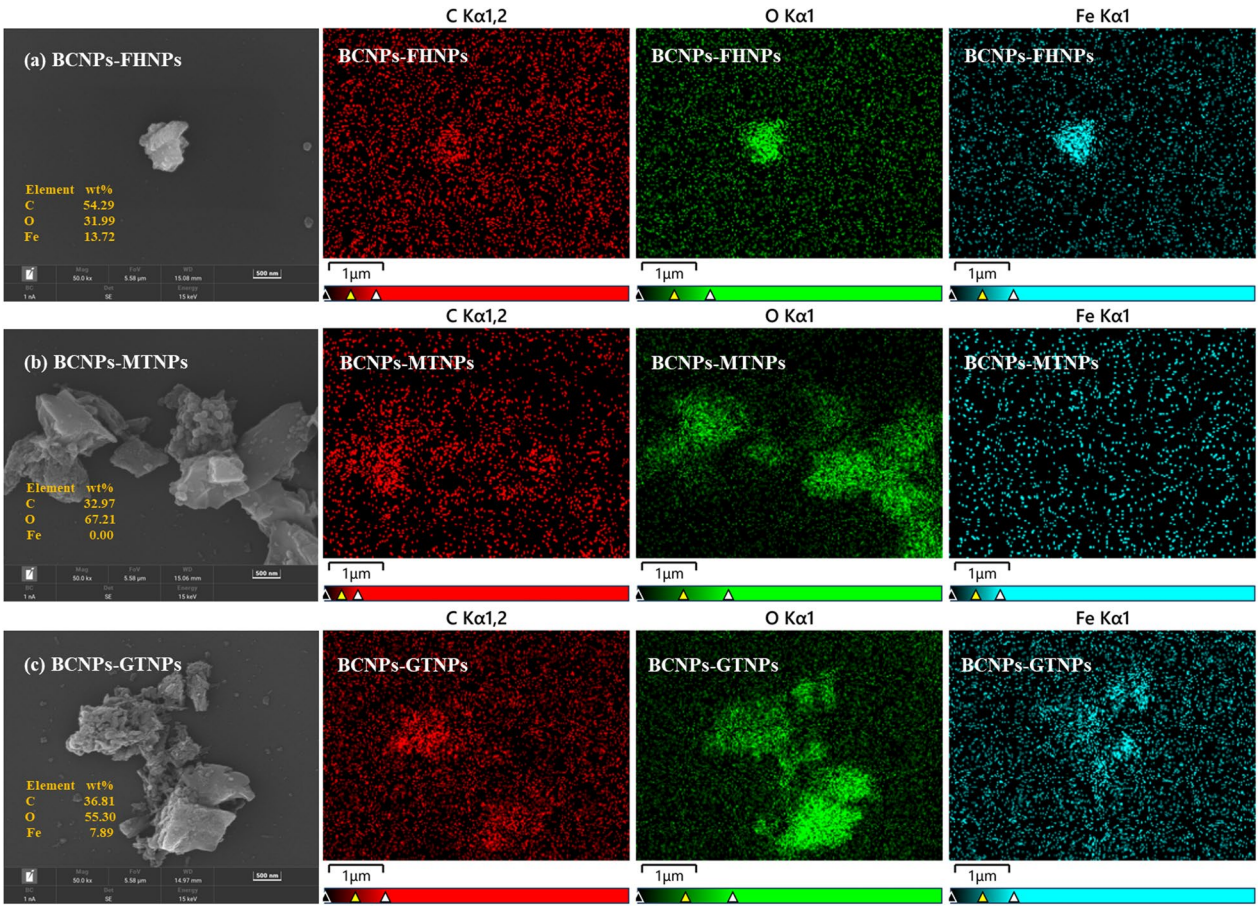

Fig. 4 Morphology and elemental mapping (red stands for C, green stands for O, and cyan stands for Fe) of BCNPs-IMNPs (BC 0.1 g and IM 0.02 g) mixed systems at pH 7.0 and at time t = 200 min

Table S3), the $C_{res'}$ value simultaneously decreased. This indicates that the decrease in the initial settling rate did not alter the characteristics of settling. The bridge action improved the overall settling amount. The V_s and $C_{res'}$ values of the BCNPs-MTNPs in the presence of FA were 1.26 mm h^{-1} and 0.738 (Fig. 3b and Additional file 1: Table S4), respectively, indicating that FA had a slight inhibitory effect on the settling of BCNPs-MTNPs. The settling characteristics of BCNPs-MTNPs in the presence of IS and the coexistence of IS and HA were similar to those of BCNPs-FHNPs (Fig. 3a and b). In general, the settling rate of BCNPs-MTNPs was higher than that of BCNPs-FHNPs under various conditions, indicating that the BCNPs-MTNPs were relatively unstable. However, the effect of HA and IS on the settling of BCNPs-MTNPs was weaker than that of BCNPs-FHNPs (Fig. 3a and b).

The settling of BCNPs-GTNPs under different conditions showed an apparent discrepancy (Fig. 3c) similar to that at different pH values (Fig. 3c). Because the settling of BCNPs-GTNPs was very slow under the three conditions of HA, FA, and 10 mM IS with HA, we did not obtain their fitting parameters. Perhaps because of the high GTNPs concentration, the bridging effect of HA was not observed. In the presence of 10 mM IS, the $C_{res'}$ values of the BCNPs-GTNPs were close to 0 (0.053) (Additional file 1: Table S4), indicating that the BCNPs-GTNPs deposition was very thorough. The settling of BCNPs-GTNPs was similar to that of BCNPs-FHNPs under 100 mM IS with HA (Fig. 3a and c), and its V_s and $C_{res'}$ values were 3.15 mm h^{-1} and 0.430, respectively (Additional file 1: Table S4). The large particle size (690.6 and 1291.0 nm, Additional file 1: Table S1) also contributed to the rapid settling. Meanwhile, the DLVO calculation results for the BCNPs-GTNPs systems did not correspond well with settlement characteristics (Fig. 3c and f). Such failures have also been observed at different pH values (Fig. 2c and f), which are strongly dependent on morphology of nanoparticle (Han et al. 2006). The different properties of the two ends of the mirror image in non-circular nanoparticles readily cause surface

heterogeneity, which occurred readily in GTNPs owing to their elongated morphology (Ma et al. 2020). Therefore, in the presence of GTNPs, enhancing heteroaggregation and settling via surface-charge heterogeneity under varying conditions was predicted to be unfavorable according to the DLVO theory (Pazmino et al. 2014; Tombácz and Szekeres 2006).

In this study, although DLVO theory can not explain the settling characteristics perfectly, the correlations between the primary energy barrier and C_{res}, in BCNPs-FHNPs ($R^2 = 0.732$) and BCNPs-MTNPs ($R^2 = 0.484$) under different iron masses and pH values were evident (Additional file 1: Fig. S2a and b). However, the corresponding correlations decreased under different environmental conditions (Additional file 1: Fig. S2). The non-DLVO forces caused by the coexistence of multiple factors (BCNPs, IMNPs, ions, and DOM) contributed significantly to settling. It is generally believed that the adsorption of DOM, especially HA, on nanoparticles produces steric repulsion, which keeps nanoparticles stable (Ma et al. 2018; Philippe and Schaumann 2014; Xu et al. 2021). However, in the present study, HA did not stabilize the BCNPs or BCNPs-IMNPs, and the effect of steric repulsion was limited. By contrast, bridging HA and ions can promote settling (Li and Sun 2011). Different environmental conditions (different pH, IS, and DOM) have very different effects on the stability of different BCNPs-IMNPs, and it is difficult to find a consistent rule. We speculated that the stability of BCNPs-IMNPs are related to the interactions between BCNPs and IMNPs.

3.4 Interaction of BCNPs-IMNPs and influence on their stability

The SEM images of individual BCNPs and IMNPs are shown in Additional file 1: Fig. S4. The percentage of C (54.29%), O (31.99%), and Fe (13.72%) were observed simultaneously and uniformly on the BCNPs-FHNPs (Fig. 4a), which suggested an intimate interaction between BCNPs and FHNPs. However, in the BCNPs-MTNPs system, the absence of Fe (Fig. 4b and Additional file 1: Fig. S5) resulted in the possible separation of BCNPs and MTNPs. Some previous studies have reported that MTNPs can easily combine with bulk BC via binding with the rough surface or the pores of BC (Chen et al. 2022a; Liu et al. 2022a). However, it is difficult for electronegative MTNPs and BCNPs to combine under neutral conditions owing to the low point of zero charge (6.5) of MTNPs (Milonjić et al. 1983). However, a different connection was observed in the BCNPs-GTNPs system, where C, O, and Fe elements only coexisted in the upper half skeleton of BCNPs-GTNPs, and C and O signals were exhibited by the lower half (Fig. 4c). A previous study reported a clear complexation between BCNPs and GTNPs (Gui et al. 2021). Therefore, we speculated that the order of interactions between IMNPs and BCNPs was: FHNPs > GTNPs > MTNPs.

Quantum chemical computations are widely used to investigate the behavior of nanoparticles (Cortes-Arriagada 2021; Ma et al. 2022; Ray et al. 2022; Yasir et al. 2022). In this study, quantum chemical computations were used to investigate the interaction between BCNPs and IMNPs. In the BCNPs-FHNPs system, the molecular configuration of BC was almost parallel to the FH crystal structure (Fig. 5a). Therefore, the area of interaction between the two structures was large, further producing strong van der Waals interactions (I_{VDW}). The short distance of C atoms in the BCNPs molecules between Fe atoms in FHNPs caused approximate covalent bond interaction, leading to strong adsorption. The electrostatic potential surfaces of the two molecules penetrate each other more clearly. The penetration distances in areas A and B were 2.239 and 1.736 Å, respectively (Additional file 1: Table S5). As several C atoms in BCNPs interact strongly with Fe atoms, the binding energy is very large (−2755.58 kJ mol^{-1}) (Additional file 1: Table S6).

In the BCNPs-MTNPs system, the binding energy between BCNPs molecular and crystal structure of MTNPs was −1676.73 kJ mol^{-1} (Additional file 1: Table S6), and the interaction occurred at the edge of the crystal structure of MTNPs (Fig. 5b). The penetration distances in areas A and B were 1.767 and 1.049 Å, respectively (Additional file 1: Table S5). In the BCNPs-GTNPs system, a small angle between the BC molecular configuration and the crystal structure of GT (Fig. 5c) caused a smaller I_{VDW} than that in BCNPs-FHNPs. However, strong covalent bonds were formed between C and Fe or O and Fe, confirmed by a small atomic distance (~2.0 Å). Moreover, obvious penetrating phenomena were observed in areas A and B, with penetrating distances of 2.145 and 1.007 Å, respectively (Additional file 1: Table S5). In particular, in area A, the H atom on the BC molecule was transferred to the O atom on the surface of the GTNPs, resulting in a good combination between the two molecules. Overall, the binding energy between the molecular and crystal structures of GTNPs was −1706.23 kJ mol^{-1}, which was slightly higher than that in the BCNPs-MTNPs system (Additional file 1: Table S6). The electrostatic potential distribution on the surface of the IMNPs was symmetrical, nearly neutral, and slightly negative. However, the BCNPs molecule exhibited a clear negative potential on its surface, owing to the presence of a benzene ring and O atoms. The hydroxyl and carboxyl groups of the BCNPs were also combined with the positively charged IMNPs (Gui et al. 2021). The difference in charge between the BCNPs and IMNPs facilitated the

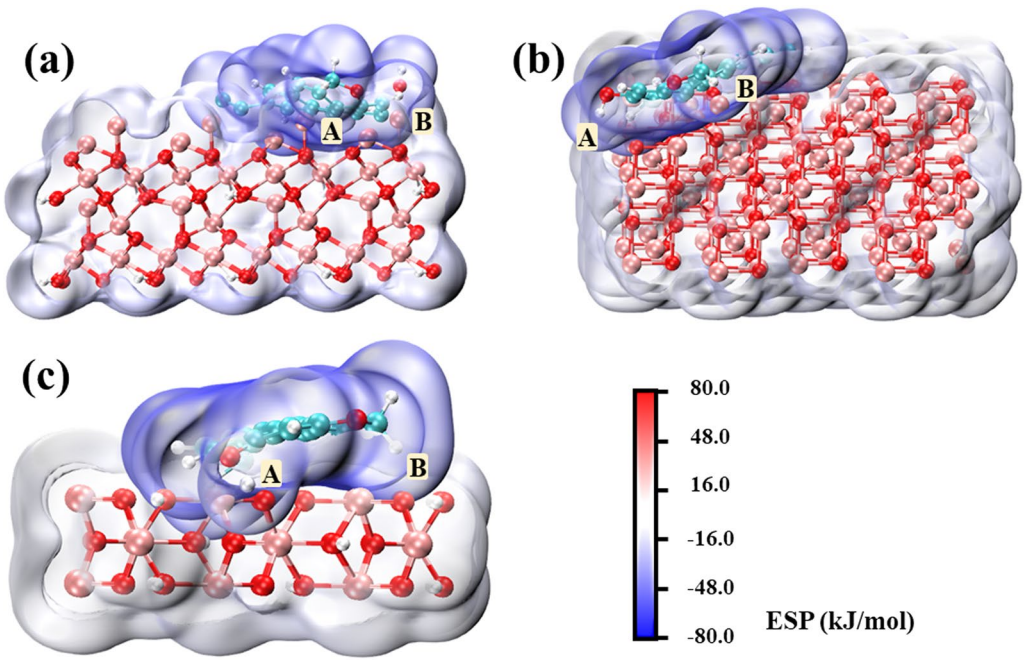

Fig. 5 Cluster model of the structures of BCNPs and IMNPs: BCNPs-FHNPs (**a**), BCNPs-MTNPs (**b**), and BCNPs-GTNPs (**c**). The blue-green, white, red, and pink spheres represent C, O, H, and Fe, respectively. ESP indicates the electrostatic potential of the macromolecule, wherein red and blue are the positive and negative areas, respectively. Two key regions (A and B) were identified for each cluster model. Their vertex coordinates and interpenetration distances are shown in Additional file 1: Table S5. The binding energies between the BCNPs and IMNPs are shown in Additional file 1: Table S6

interaction between these molecules, whereas the crystal structure of IMNPs determined the magnitude of this interaction. The amorphous FHNPs had the highest ESP, whereas the ESP values of the highly crystalline GTNPs and MTNPs were relatively low. However, in the suspension system, the concentration of GTNPs was much higher than that of MTNPs, whereas the interaction between BCNPs and MTNPs tended to occur towards the edges of the molecules. Hence, the likelihood of a combination of BCNPs and MTNPs was lower than that of BCNPs and GTNPs; this observation is consistent with the SEM observations of the present study.

The pH and IS of a solution, which is a function of the concentration of H^+ (OH^-) and all dissolved ions, play a crucial role in the stability of nanoparticles by affecting their surface charge and, hence, their potential propensity to aggregate (Van Koetsem et al. 2015). The aggregation behavior of colloids is also influenced by DOM (Wang et al. 2022; Yang et al. 2019). These environmental conditions affect the settling of nanoparticles by changing their electrical properties, the compression of the electrical double layer, and interparticle bridging. We speculated that the interaction between BCNPs and IMNPs had a significant effect on the settling response under unfavorable conditions. For example, strong interactions between BCNPs and FHNPs caused loss of stability under conditions of 10 mg L^{-1} HA at pH 7.0 and 10 mg L^{-1} HA-100 IS at pH 7.0 and at pH 4.0 compared with that at pH 7.0. Strong interactions can likely promote the settling in unfavorable conditions owing to the ease of forming complex structure via bridging. However, this effect is not evident in the BCNPs-MTNPs system owing to the weak interactions of BCNPs and MTNPs. The unfavorable conditions, such as presence of HA and high IS, caused low heteroaggregation owing to the lack of incentive to form complex structures. The relatively weak interaction between BCNPs and GTNPs was similar to that between BCNPs and MTNPs. However, the settling characteristics were quite different under different environmental conditions. This was probably due to the presence of more GTNPs in the suspension (Additional file 1: Table S1). The high concentration and elongated structure of the GTNPs contributed to settling of the nanoparticles; moreover, the weak interactions cannot be ignored. The findings of the present study are of great significance and can be used in the engineering applications of composite nanomaterials.

4 Conclusion

In the present study, the combined effects of the interaction of BCNPs-IMNPs and environmental conditions on the aggregation and settling behavior of a mixture of nanoparticles were determined. The results of this study showed that the settling of BCNPs-FHNPs and BCNPs-GTNPs exhibited polarized characteristics. As BCNPs provided high negative potential, a relatively stable state of nanoparticles at neutral and alkaline pH was observed in the BCNPs-FHNPs and BCNPs-GTNPs systems. However, acidic conditions readily caused fast settling of nanoparticles. BCNPs-MTNPs consistently showed moderate settling regardless of the mass of MT at all pH values. The SEM and quantum chemical calculation results suggested that the interaction between BCNPs and FHNPs was stronger than that between BCNPs and GTNPs/MTNPs. The binding energies of the BCNPs-MTNPs and BCNPs-GTNPs systems were similar. The interaction between BCNPs and IMNPs enhanced heteroaggregation under unfavorable conditions (acidic pH, HA, and IS). The strength of the interaction regulates the change in the enhancement of heteroaggregation. The results of the present study elucidate the quantum and colloidal chemical-interface mechanisms between BCNPs and IMNPs in soil. However, the present study only selected common environmental conditions as influencing factors, which may not fully reflect the real environment. Therefore, the stability of BCNPs-MTNPs in the soil pore environment needs to be further studied. In particular, the influence of various soil solution ions, clay minerals, and plant root exudates on the stability of BCNPs-MTNPs should be explored in future.

Supplementary Information

The online version contains supplementary material available at https://doi.org/10.1007/s42773-022-00172-z.

Additional file 1. Supplementary Material.

Acknowledgements
Not applicable.

Authors contributions
YL: formal analysis, writing—original draft and writing—review and editing. JM: formal analysis, writing—original draft, writing—review and editing, methodology, and visualization. JG: investigation. XC: investigation. XO: writing—review and editing. LW: supervision and project administration. HL: supervision. YC: project administration. YL: funding acquisition. All authors read and approved the final manuscript.

Funding
The study is financially supported by the National Natural Science Foundation of China (No. 41701262) and Key Projects at the Institute of Innovation Engineering.

Availability of data and materials
Not applicable.

Declarations

Ethics approval and consent to participate
Informed consent was obtained from all individual participants included in the study.

Consent to publication
Authors are responsible for correctness of the statements provided in the manuscript. The publication has been approved by all co-authors.

Competing interests
The authors declare no potential conflict of interest. The authors declare that they have no known competing financial interests or personal relationships that could have appeared to influence the work reported in this paper.

Author details
[1]Key Laboratory for Environmental Factors Control of Agro-Product Quality Safety, Ministry of Agriculture and Rural Affairs, Tianjin 300191, China. [2]Agro-Environmental Protection Institute, Ministry of Agriculture and Rural Affairs, Tianjin 300191, China. [3]Institute of Resources and Environmental Engineering, Shanxi University, Taiyuan 030006, Shanxi, China. [4]Department of Soil Quality, Wageningen University, Wageningen, The Netherlands. [5]College of Marine and Environmental Science, Tianjin University of Science and Technology, Tianjin 300457, China. [6]College of Resource and Environmental Engineering, Jiangxi University of Science and Technology, Ganzhou 341000, Jiangxi, China. [7]College of Natural Resources and Environment, South China Agricultural University, Guangzhou 510642, China.

Received: 21 April 2022 Accepted: 12 July 2022
Published online: 27 July 2022

References

Ahmad M, Lee SS, Dou X, Mohan D, Sung JK, Yang JE, Ok YS (2012) Effects of pyrolysis temperature on soybean stover- and peanut shell-derived biochar properties and TCE adsorption in water. Bioresourse Technol 118:536–544. https://doi.org/10.1016/j.biortech.2012.05.042

Angelico R, Ceglie A, He JZ, Liu YR, Palumbo G, Colombo C (2014) Particle size, charge and colloidal stability of humic acids coprecipitated with Ferrihydrite. Chemosphere 99:239–247. https://doi.org/10.1016/j.chemosphere.2013.10.092

Baragaño D, Alonso J, Gallego JR, Lobo MC, Gil-Díaz M (2020) Magnetite nanoparticles for the remediation of soils co-contaminated with As and PAHs. Chem Eng J 399:125809. https://doi.org/10.1016/j.cej.2020.125809

Blakey BC, James DF (2003) The viscous behaviour and structure of aqueous suspensions of goethite. Colloids Surfaces A 231(1–3):19–30. https://doi.org/10.1016/j.colsurfa.2003.08.019

Buske N (1994) Application of magnetite sols in environmental technology. Prog Polym Sci 95:175–180. https://doi.org/10.1007/BFb0115720

Chappell HF, Thom W, Bowron DT, Faria N, Hasnip PJ, Powell JJ (2017) Structure of naturally hydrated ferrihydrite revealed through neutron diffraction and first-principles modeling. Phys Rev Mater. https://doi.org/10.1103/PhysRevMaterials.1.036002

Chen M, Wang D, Yang F, Xu X, Xu N, Cao X (2017) Transport and retention of biochar nanoparticles in a paddy soil under environmentally-relevant solution chemistry conditions. Environ Pollut 230:540–549. https://doi.org/10.1016/j.envpol.2017.06.101

Chen M, Alim N, Zhang Y, Xu N, Cao X (2018) Contrasting effects of biochar nanoparticles on the retention and transport of phosphorus in acidic and alkaline soils. Environ Pollut 239:562–570. https://doi.org/10.1016/j.envpol.2018.04.050

Chen Y, Ma J, Li Y, Weng L (2019) Enhanced cadmium immobilization in saturated media by gradual stabilization of goethite in the presence of humic acid with increasing pH. Sci Total Environ 648:358–366. https://doi.org/10.1016/j.scitotenv.2018.08.086

Chen X, Dai Y, Fan J, Xu X, Cao X (2021) Application of iron-biochar composite in topsoil for simultaneous remediation of chromium-contaminated soil and groundwater: immobilization mechanism and long-term stability. J Hazard Mater 405:124226. https://doi.org/10.1016/j.jhazmat.2020.124226

Chen J, Zhang P, Zhang J, He Y, Tong YW (2022a) Micro-nano magnetite-loaded biochar enhances interspecies electron transfer and viability of functional microorganisms in anaerobic digestion. ACS Sustain Chem Eng 10(8):2811–2821. https://doi.org/10.1021/acssuschemeng.1c08288
Chen M, Wang D, Xu X, Zhang Y, Gui X, Song B, Xu N (2022b) Biochar nanoparticles with different pyrolysis temperatures mediate cadmium transport in water-saturated soils: effects of ionic strength and humic acid. Sci Total Environ 806(2):150668. https://doi.org/10.1016/j.scitotenv.2021.150668
Clarr van der Zee C, Roberts DR, Rancourt DG, Slomp CP (2003) Nanogoethite is the dominant reactive oxyhydroxide phase in lake and marine sediments. Geology 31(11):993. https://doi.org/10.1130/g19924.1
Cortes-Arriagada D (2021) Elucidating the co-transport of bisphenol A with polyethylene terephthalate (PET) nanoplastics: a theoretical study of the adsorption mechanism. Environ Pollut 270:116192. https://doi.org/10.1016/j.envpol.2020.116192
Derjaguin B, Landau L (1993) Theory of the stability of strongly charged lyophobic sols and of the adhesion of strongly charged particles in solutions of electrolytes. Prog Surf Sci 43(1–4):30–59. https://doi.org/10.1016/0079-6816(93)90013-l
Dublet G, Lezama Pacheco J, Bargar JR, Fendorf S, Kumar N, Lowry GV, Brown GE (2017) Partitioning of uranyl between ferrihydrite and humic substances at acidic and circum-neutral pH. Geochim Cosmochim Ac 215:122–140. https://doi.org/10.1016/j.gca.2017.07.013
Dwivedi AD, Ma LQ (2014) Biocatalytic synthesis pathways, transformation, and toxicity of nanoparticles in the environment. Crit Rev Env Sci Tec 44(15):1679–1739. https://doi.org/10.1080/10643389.2013.790747
Fang J, Zhang K, Sun P, Lin D, Shen B, Luo Y (2016) Co-transport of Pb(2+) and TiO2 nanoparticles in repacked homogeneous soil columns under saturation condition: effect of ionic strength and fulvic acid. Sci Total Environ 571:471–478. https://doi.org/10.1016/j.scitotenv.2016.07.013
Frisch MJ, Trucks GW, Schlegel HB, Scuseria GE, Robb MA, Cheeseman JR, Scalmani G, Barone V, Petersson GA, Nakatsuji H, Li X, Caricato M, Marenich AV, Bloino J, Janesko BG, Gomperts R, Mennucci B, Hratchian HP, Ortiz JV, Izmaylov AF, Sonnenberg JL, Williams-Young D, Ding F, Lipparini F, Egidi F, Goings J, Peng B, Petrone A, Henderson T, Ranasinghe D, Zakrzewski VG, Gao J, Rega N, Zheng G, Liang W, Hada M, Ehara M, Toyota K, Fukuda R, Hasegawa J, Ishida M, Nakajima T, Honda Y, Kitao O, Nakai H, Vreven T, Throssell K, Jr. Montgomery J A, Peralta JE, Ogliaro F, Bearpark MJ, Heyd JJ, Brothers EN, Kudin KN, Staroverov VN, AK T, Kobayashi R, Normand J, Raghavachari K, Rendell A P, Burant J C, Iyengar SS, Tomasi J, Cossi M, Millam JM, Klene M, Adamo C, Cammi R, Ochterski J W, Martin RL, Morokuma K, Farkas O, Foresman J B, Fox DJ (2016) Gaussian 16, Revision B.01, Gaussian, Inc., Wallingford CT
Gholizadeh M, Hu X (2021) Removal of heavy metals from soil with biochar composite: a critical review of the mechanism. J Environ Chem Eng 9(5):105830. https://doi.org/10.1016/j.jece.2021.105830
Gregory J (1981) Approximate expressions for retarded van der waals interaction. J Colloid Interf Sci 83(1):138–145. https://doi.org/10.1016/0021-9797(81)90018-7
Gui X, Song B, Chen M, Xu X, Ren Z, Li X, Cao X (2021) Soil colloids affect the aggregation and stability of biochar colloids. Sci Total Environ 771:145414. https://doi.org/10.1016/j.scitotenv.2021.145414
Han Y, Alsayed AM, Nobili M, Zhang J, Lubensky TC, Yodh AG (2006) Brownian motion of an ellipsoid. Science 314(5799):626–630. https://doi.org/10.1126/science.1130146
Hotze EM, Phenrat T, Lowry GV (2010) Nanoparticle aggregation: challenges to understanding transport and reactivity in the environment. J Environ Qual 39(6):1909–1924. https://doi.org/10.2134/jeq2009.0462
Hu JD, Zevi Y, Kou XM, Xiao J, Wang XJ, Jin Y (2010) Effect of dissolved organic matter on the stability of magnetite nanoparticles under different pH and ionic strength conditions. Sci Total Environ 408(16):3477–3489. https://doi.org/10.1016/j.scitotenv.2010.03.033
Humphrey W, Dalke A, Schulten K (1996) VMD: visual molecular dynamics. J Mol Grap 14(1):33–38. https://doi.org/10.1016/0263-7855(96)00018-5
Irshad MK, Noman A, Alhaithloul HAS, Adeel M, Rui Y, Shah T, Zhu S, Shang J (2020) Goethite-modified biochar ameliorates the growth of rice (Oryza sativa L.) plants by suppressing Cd and As-induced oxidative stress in Cd and As co-contaminated paddy soil. Sci Total Environ 717:137086. https://doi.org/10.1016/j.scitotenv.2020.137086
Islam MA, Morton DW, Johnson BB, Angove MJ (2020) Adsorption of humic and fulvic acids onto a range of adsorbents in aqueous systems, and their effect on the adsorption of other species: a review. Sep Purif Tech 247:116949. https://doi.org/10.1016/j.seppur.2020.116949
Ivanić M, Škapin S, Vdović N, Mikac N, Sondi I (2016) Size dependent physico-chemical and geochemical characteristics of two distinct carbonate-Rrch marine sediments (Adriatic Sea), pp. 105–106
Joseph SD, Camps-Arbestain M, Lin Y, Munroe P, Chia CH, Hook J, Zwieten LV, Kimber S, Cowie A, Singh BP, Lehmann J, Foidl N, Smernik RJ, Amonette JE (2010) An investigation into the reactions of biochar in soil. Aust J Soil Res 48(7):501–515. https://doi.org/10.1071/SR10009
Jung KW, Lee SY, Lee YJ (2018) Hydrothermal synthesis of hierarchically structured birnessite-type MnO2/biochar composites for the adsorptive removal of Cu(II) from aqueous media. Bioresourse Tech 260:204–212. https://doi.org/10.1016/j.biortech.2018.03.125
Kappler A, Wuestner ML, Ruecker A, Harter J, Halama M, Behrens S (2014) Biochar as an electron shuttle between bacteria and Fe(III) minerals. Environ Sci Tech Let 1(8):339–344. https://doi.org/10.1021/ez5002209
Klucakova M (2018) Size and charge evaluation of standard humic and fulvic acids as crucial factors to determine their environmental behavior and impact. Front Chem 6:235. https://doi.org/10.3389/fchem.2018.00235
Li S, Sun W (2011) A comparative study on aggregation/sedimentation of TiO2 nanoparticles in mono- and binary systems of fulvic acids and Fe(III). J Hazard Mater 197:70–79. https://doi.org/10.1016/j.jhazmat.2011.09.059
Lin D, Tian X, Wu F, Xing B (2010) Fate and transport of engineered nanomaterials in the environment. J Environ Qual 39(6):1896–1908. https://doi.org/10.2134/jeq2009.0423
Liu H, Seifert G, Di Valentin C (2019a) An efficient way to model complex magnetite: assessment of SCC-DFTB against DFT. J Chem Phys 150(9):094703. https://doi.org/10.1063/1.5085190
Liu J, Louie SM, Pham C, Dai C, Liang D, Hu Y (2019b) Aggregation of ferrihydrite nanoparticles: effects of pH, electrolytes, and organics. Environ Res 172:552–560. https://doi.org/10.1016/j.envres.2019.03.008
Liu Q, Sheng Y, Wang W, Li C, Zhao G (2020) Remediation and its biological responses of Cd contaminated sediments using biochar and minerals with nanoscale zero-valent iron loading. Sci Total Environ 713:136650. https://doi.org/10.1016/j.scitotenv.2020.136650
Liu C, Ma J, Wang L, Chen Y, Weng L, Li Y (2022a) The pore blocking effect decreases the cadmium adsorption onto biochar-magnetite complex. Acta Sci Circum 41(10):4140–4149
Liu M, Almatrafi E, Zhang Y, Xu P, Song B, Zhou C, Zeng G, Zhu Y (2022b) A critical review of biochar-based materials for the remediation of heavy metal contaminated environment: applications and practical evaluations. Sci Total Environ 806:150531. https://doi.org/10.1016/j.scitotenv.2021.150531
Lu T (2021) Molclus Program, Version 1.9.9.6. http://www.keinsci.com/research/molclus.html, accessed Sep-4
Lu T, Chen F (2012) Multiwfn: a multifunctional wavefunction analyzer. J Comput Chem 33(5):580–592. https://doi.org/10.1002/jcc.22885
Lu HP, Li ZA, Gasco G, Mendez A, Shen Y, Paz-Ferreiro J (2018) Use of magnetic biochars for the immobilization of heavy metals in a multi-contaminated soil. Sci Total Environ 622–623:892–899. https://doi.org/10.1016/j.scitotenv.2017.12.056
Ma S, Zhou K, Yang K, Lin D (2015) Heteroagglomeration of oxide nanoparticles with algal cells: effects of particle type, ionic strength and pH. Environ Sci Technol 49(2):932–939. https://doi.org/10.1021/es504730k
Ma J, Guo H, Lei M, Li Y, Weng L, Chen Y, Ma Y, Deng Y, Feng X, Xiu W (2018) Enhanced transport of ferrihydrite colloid by chain-shaped humic acid colloid in saturated porous media. Sci Total Environ 621:1581–1590. https://doi.org/10.1016/j.scitotenv.2017.10.070
Ma J, Jing Y, Gao L, Chen J, Wang Z, Weng L, Li H, Chen Y, Li Y (2020) Heteroaggregation of goethite and ferrihydrite nanoparticles controlled by goethite nanoparticles with elongated morphology. Sci Total Environ 748:141536. https://doi.org/10.1016/j.scitotenv.2020.141536
Ma J, Qiu Y, Zhao J, Ouyang X, Zhao Y, Weng L, Yasir AM, Chen Y, Li Y (2022) Effect of agricultural organic inputs on nanoplastics transport in saturated goethite-coated porous media: particle size selectivity and role of dissolved organic matter. Environ Sci Technol 56(6):3524–3534. https://doi.org/10.1021/acs.est.1c07574

Milonjić SK, Kopečni MM, Ilić ZE (1983) The point of zero charge and adsorption properties of natural magnetite. J Radioanalytical Chem 78(1):15–24. https://doi.org/10.1007/bf02519745
Mitrano DM, Motellier S, Clavaguera S, Nowack B (2015) Review of nanomaterial aging and transformations through the life cycle of nano-enhanced products. Environ Int 77:132–147. https://doi.org/10.1016/j.envint.2015.01.013
Nielsen SS, Kjeldsen P, Hansen HCB, Jakobsen R (2014) Transformation of natural ferrihydrite aged in situ in As, Cr and Cu contaminated soil studied by reduction kinetics. Appl Geochem 51:293–302. https://doi.org/10.1016/j.apgeochem.2014.10.014
O'Connor D, Peng T, Zhang J, Tsang DCW, Alessi DS, Shen Z, Bolan NS, Hou D (2018) Biochar application for the remediation of heavy metal polluted land: a review of in situ field trials. Sci Total Environ 619–620:815–826. https://doi.org/10.1016/j.scitotenv.2017.11.132
Ouyang X, Ma J, Li P, Chen Y, Weng L, Li Y (2021) Comparison of the effects of large-grained and nano-sized biochar, ferrihydrite, and complexes thereof on Cd and As in a contaminated soil-plant system. Chemosphere 280:130731. https://doi.org/10.1016/j.chemosphere.2021.130731
Pazmino E, Trauscht J, Dame B, Johnson WP (2014) Power law size-distributed heterogeneity explains colloid retention on soda lime glass in the presence of energy barriers. Langmuir 30(19):5412–5421. https://doi.org/10.1021/la501006p
Philippe A, Schaumann GE (2014) Interactions of dissolved organic matter with natural and engineered inorganic colloids: a review. Environ Sci Technol 48(16):8946–8962. https://doi.org/10.1021/es502342r
Qian X, Ma J, Weng L, Chen Y, Ren Z, Li Y (2020) Influence of agricultural organic inputs and their aging on the transport of ferrihydrite nanoparticles: from enhancement to inhibition. Sci Total Environ 719:137440. https://doi.org/10.1016/j.scitotenv.2020.137440
Qiu M, Liu L, Ling Q, Cai Y, Yu S, Wang S, Fu D, Hu B, Wang X (2022) Biochar for the removal of contaminants from soil and water: a review. Biochar 4(1):19. https://doi.org/10.1007/s42773-022-00146-1
Quik JT, Velzeboer I, Wouterse M, Koelmans AA, van de Meent D (2014) Heteroaggregation and sedimentation rates for nanomaterials in natural waters. Water Res 48:269–279. https://doi.org/10.1016/j.watres.2013.09.036
Ray M, Mandal SC, Chakrabarti J (2022) Quantum chemical studies on chelation in nano-bio conjugate between ZnO nanoparticles and cellular energy carrier molecules. Mater Chem Phys 279:125744. https://doi.org/10.1016/j.matchemphys.2022.125744
Russell B, Payne M, Ciacchi LC (2009) Density functional theory study of Fe(II) adsorption and oxidation on goethite surfaces. Phys Rev B. https://doi.org/10.1103/PhysRevB.79.165101
Schwertmann U, Stanjek H, Becher HH (2018) Long-term in vitro transformation of 2-line ferrihydrite to goethite/hematite at 4, 10, 15 and 25°C. Clay Miner 39(4):433–438. https://doi.org/10.1180/0009855043940145
Schwertmann U, Cornell RM (2008) Iron oxides in the laboratory preparation and characterization
Su H, Fang Z, Tsang PE, Zheng L, Cheng W, Fang J, Zhao D (2016) Remediation of hexavalent chromium contaminated soil by biochar-supported zero-valent iron nanoparticles. J Hazard Mater 318:533–540. https://doi.org/10.1016/j.jhazmat.2016.07.039
Tian H, He Z, Wang J, Jiao H, Hu Z, Yang Y (2020) Density functional theory study on the mechanism of biochar gasification in CO2 environment. Ind Eng Chem Res 59(45):19972–19981. https://doi.org/10.1021/acs.iecr.0c04105
Till JL, Guyodo Y, Lagroix F, Morin G, Ona-Nguema G (2015) Goethite as a potential source of magnetic nanoparticles in sediments. Geology 43(1):75–78. https://doi.org/10.1130/g36186.1
Tombácz E, Szekeres M (2006) Surface charge heterogeneity of kaolinite in aqueous suspension in comparison with montmorillonite. Appl Clay Sci 34(1–4):105–124. https://doi.org/10.1016/j.clay.2006.05.009
Tosco T, Bosch J, Meckenstock RU, Sethi R (2012) Transport of ferrihydrite nanoparticles in saturated porous media: role of ionic strength and flow rate. Environ Sci Technol 46(7):4008–4015. https://doi.org/10.1021/es202643c
Van Koetsem F, Verstraete S, Van der Meeren P, Du Laing G (2015) Stability of engineered nanomaterials in complex aqueous matrices: settling behaviour of CeO2 nanoparticles in natural surface waters. Environ Res 142:207–214. https://doi.org/10.1016/j.envres.2015.06.028
Velzeboer I, Quik JTK, van de Meent D, Koelmans AA (2014) Rapid setting of nanoparticles due to heteroaggeration with suspended ssedimnnt. Environ Toxicol 33(8):1766–1773. https://doi.org/10.1002/etc.2611
Verwey EJ (1947) Theory of the stability of lyophobic colloids. J Phys Colloid Chem 51(3):631–636. https://doi.org/10.1021/j150453a001
Vikesland PJ, Rebodos RL, Bottero JY, Rose J, Masion A (2016) Aggregation and sedimentation of magnetite nanoparticle clusters. Environ Sci: Nano 3(3):567–577. https://doi.org/10.1039/c5en00155b
Vodyanitskii YN, Shoba SA (2016) Ferrihydrite in soils. Eurasian Soil Sci 49(7):796–806. https://doi.org/10.1134/s1064229316070127
Wan X, Li C, Parikh SJ (2020) Simultaneous removal of arsenic, cadmium, and lead from soil by iron-modified magnetic biochar. Environ Pollut 261:114157. https://doi.org/10.1016/j.envpol.2020.114157
Wang D, Zhang W, Hao X, Zhou D (2013) Transport of biochar particles in saturated granular media: effects of pyrolysis temperature and particle size. Environ Sci Technol 47(2):821–828. https://doi.org/10.1021/es303794d
Wang S, Gao B, Li Y, Mosa A, Zimmerman AR, Ma LQ, Harris WG, Migliaccio KW (2015) Manganese oxide-modified biochars: preparation, characterization, and sorption of arsenate and lead. Bioresourse Technol 181:13–17. https://doi.org/10.1016/j.biortech.2015.01.044
Wang L, Li Y, Weng L, Sun Y, Ma J, Chen Y (2019) Using chromatographic and spectroscopic parameters to characterize preference and kinetics in the adsorption of humic and fulvic acid to goethite. Sci Total Environ 666:766–777. https://doi.org/10.1016/j.scitotenv.2019.02.235
Wang Y, Liu Y, Su G, Yang K, Lin D (2021) Transformation and implication of nanoparticulate zero valent iron in soils. J Hazardous Mater 412:125207. https://doi.org/10.1016/j.jhazmat.2021.125207
Wang Y, Wang C, Xiong J, Zhang Q, Shang J (2022) Effects of low molecular weight organic acids on aggregation behavior of biochar colloids at acid and neutral conditions. Biochar 4(1):20. https://doi.org/10.1007/s42773-022-00142-5
Weng L, van Riemsdijk WH, Koopal LK, Hiemstra T (2006) Adsorption of humic substances on goethite: comparison between humic acids and fulvic acids. Environ Sci Technol 40(24):7494–7500. https://doi.org/10.1021/es060777d
Xu S, Adhikari D, Huang R, Zhang H, Tang Y, Roden E, Yang Y (2016) Biochar-facilitated microbial reduction of hematite. Environ Sci Technol 50(5):2389–2395. https://doi.org/10.1021/acs.est.5b05517
Xu Z, Niu Z, Pan D, Zhao X, Wei X, Li X, Tan Z, Chen X, Liu C, Wu W (2021) Mechanisms of bentonite colloid aggregation, retention, and release in saturated porous media: role of counter ions and humic acid. Sci Total Environ 793:148545. https://doi.org/10.1016/j.scitotenv.2021.148545
Yang F, Zhao L, Gao B, Xu X, Cao X (2016) The interfacial behavior between biochar and soil minerals and its effect on biochar stability. Environ Sci Technol 50(5):2264–2271. https://doi.org/10.1021/acs.est.5b03656
Yang W, Wang Y, Sharma P, Li B, Liu K, Liu J, Flury M, Shang J (2017) Effect of naphthalene on transport and retention of biochar colloids through saturated porous media. Colloid Surface A 530:146–154. https://doi.org/10.1016/j.colsurfa.2017.07.010
Yang W, Shang J, Sharma P, Li B, Liu K, Flury M (2019) Colloidal stability and aggregation kinetics of biochar colloids: effects of pyrolysis temperature, cation type, and humic acid concentrations. Sci Total Environ 658:1306–1315. https://doi.org/10.1016/j.scitotenv.2018.12.269
Yasir AM, Ma J, Ouyang X, Zhao J, Zhao Y, Weng L, Islam MS, Chen Y, Li Y (2022) Effects of selected functional groups on nanoplastics transport in saturated media under diethylhexyl phthalate co-contamination conditions. Chemosphere 286:131965. https://doi.org/10.1016/j.chemosphere.2021.131965
Zhang W, Niu JZ, Morales VL, Chen XC, Hay AG, Lehmann J, Steenhuis TS (2010) Transport and retention of biochar particles in porous media: effect of pH, ionic strength, and particle size. Ecohydrology 3(4):497–508. https://doi.org/10.1002/eco.160
Zhang Q, Appel E, Hu S, Pennington RS, Meyer J, Neumann U, Burchard M, Allstädt F, Wang L, Koutsodendris A (2020) Nano-Magnetite aggregates in red soil on low magnetic bedrock, their changes during source-sink transfer, and implications for paleoclimate studies. J Geophys Res-Sol Ea. https://doi.org/10.1029/2020jb020588
Zhao W, Walker SL, Huang Q, Cai P (2014) Adhesion of bacterial pathogens to soil colloidal particles: influences of cell type, natural organic matter, and

solution chemistry. Water Res 53:35–46. https://doi.org/10.1016/j.watres.2014.01.009

Zhou D-M, Jin S-Y, Wang Y-J, Wang P, Weng N-Y, Wang Y (2012) Assessing the impact of iron-based nanoparticles on pH, dissolved organic carbon, and nutrient availability in soils. Soil Sediment Contam 21(1):101–114. https://doi.org/10.1080/15320383.2012.636778

Zhu S, Zhao J, Zhao N, Yang X, Chen C, Shang J (2020) Goethite modified biochar as a multifunctional amendment for cationic Cd(II), anionic As(III), roxarsone, and phosphorus in soil and water. J Clean Prod 247:119579. https://doi.org/10.1016/j.jclepro.2019.119579